RSC Advances

PAPER

View Article Online
View Journal | View Issue

Cite this: *RSC Adv.*, 2016, **6**, 46915

The role of sol–gel chemistry in the low-temperature formation of ZnO buffer layers for polymer solar cells with improved performance†

Giovanni Iannaccone,[a] Andrea Bernardi,[b] Raffaella Suriano,[a] Claudia L. Bianchi,[c] Marinella Levi,[a] Stefano Turri[a] and Gianmarco Griffini*[a]

A new approach is proposed in this work to chemically control the low-temperature sol–gel formation of ZnO thin films used as efficient electron transporting layers (ETLs) in inverted polymer solar cells (PSCs). The chemical composition of the ZnO sol–gel precursor was modified by systematically employing different $[H_2O]/[Zn^{2+}]$ molar ratios in the starting sol formulation and evaluating their influence on film properties and PSC device performance. A thorough characterization of the obtained ZnO ETLs evidenced the key importance of the $[H_2O]/[Zn^{2+}]$ molar ratio to achieve effective control on the sol–gel hydrolysis and condensation processes. Based on these evidences, a mechanism for the formation of the ZnO films at the low processing temperatures used in this work was proposed. PSC devices were fabricated incorporating ZnO ETLs obtained from ZnO sol precursor formulations with increasing $[H_2O]/[Zn^{2+}]$ ratios and their photovoltaic characterization revealed the presence of a maximum device efficiency for intermediate $[H_2O]/[Zn^{2+}]$ values. Finally, the effect of water in the ZnO sol precursor on the long-term (>1000 h) shelf-life of PSCs fabricated onto flexible PET substrates was investigated and a correlation was found between chemical composition of the ZnO sol precursor and device shelf-life. The results of this study give a clear demonstration of a viable strategy to achieve improved PSC device performance by chemically controlling the formation of the sol–gel based ZnO ETL at processing temperatures compatible with flexible plastic substrates and provide useful guidelines for the development of efficient sol–gel derived metal-oxide buffer layers for highly performing flexible photovoltaics.

Received 4th February 2016
Accepted 29th April 2016

DOI: 10.1039/c6ra03344j

www.rsc.org/advances

Introduction

The main driving force that has propelled scientific progress in the field of polymer solar cells (PSCs) over the past 25 years is the possibility to fabricate low-cost, lightweight, and flexible devices by means of all solution-based, large-scale roll-to-roll (R2R) processing technologies.[1–5]

In the so-called inverted architecture, efficient collection and extraction of charges at the electrodes is guaranteed by the presence of an electron transporting layer (ETL) and a hole transporting layer (HTL) that are interposed between the photoactive layer and the respective electron-collecting (typically indium–tin oxide – ITO) and hole-collecting (typically a high-work-function metal such as silver) electrodes.[6] The main requirements for the ETL in inverted PSCs are efficient electron transport and hole-blocking properties, transparency in the visible wavelength range, chemical stability, and the potential to ensure ohmic contact with the electron accepting phase of the bulk heterojunction (BHJ) in order to avoid energy barriers at the ITO interface. Such requirements can be fulfilled by n-type metal oxide thin films, such as titanium oxide (TiO_x) and zinc oxide (ZnO).[7]

In particular, ZnO is widely employed as ETL in inverted PSCs, due to its high transparency, high electron mobility, solution-processability, excellent chemical stability and inertness, nontoxicity, and appropriate energy level alignment between its conduction band minimum (about −4 eV) and the lowest unoccupied molecular orbital (LUMO) level of the electron-accepting fullerene, the latter playing a key role in the collection of photogenerated electrons.[8,9] Despite the large number of techniques successfully employed for the deposition of ZnO films,[10–14] solution-based processing remains one of the most suitable approaches in view of the high throughput requirements typical of R2R fabrication. To this end, two main strategies have been employed in the literature, namely direct deposition of crystalline nanoparticle-based ZnO suspensions and sol–gel chemistry.[15–17]

[a]*Department of Chemistry, Materials and Chemical Engineering "Giulio Natta", Politecnico di Milano, Piazza Leonardo da Vinci 32, 20133 Milano, Italy. E-mail: gianmarco.griffini@polimi.it; Tel: +39 02 2399 3213*

[b]*ENI S.p.A., Research Center for Renewable Energies & Environment – Istituto Donegani, Via Giacomo Fauser 4, 28100 Novara, Italy*

[c]*Department of Chemistry, Università degli Studi di Milano, Via Camillo Golgi 19, 20133 Milano, Italy*

† Electronic supplementary information (ESI) available. See DOI: 10.1039/c6ra03344j

More specifically, sol–gel processes are particularly useful to produce ZnO solid films in a simple, low-cost and highly controlled way, starting from a colloidal suspension (the so-called sol) prepared with an appropriate molecular precursor. Typically, hydrated organic/inorganic zinc salts (acetate, nitrate, perchlorate) are employed as metal precursors, which are dissolved in appropriate solvents such as methanol, ethanol, and 2-methoxyethanol (2-ME), in the presence of a chelating and stabilizing ligand (in most cases, monoethanolamine – MEA).[18] Zinc acetate dihydrate $Zn(CH_3COO)_2 \cdot 2H_2O$ (ZAD) is by far the most widely employed molecular precursor for the preparation of sol–gel based ZnO films in the PSC field.[19] Indeed, together with its practical advantages such as low cost, ease of handling, and widespread availability,[20] ZAD allows an easy removal of contaminants (*viz.* acetate groups) in the forming gel that can decompose during the sol–gel annealing process and can leave the ZnO film as volatile by-products, in contrast with precursors based on inorganic salts that produce ZnO films containing anionic residues more difficult to remove.[21]

The optimization of the chemical composition of the sol precursor solution represents a key step to tailor the functional properties of the resulting solid films, which in turn inevitably affect the operational performance of the PSC system. To this end, several works have appeared in the literature investigating the effect of synthetic conditions of the ZnO sol on film formation and device performance, with a major focus on the influence of the concentration of Zn salts[22–24] and stabilizing ligands[25,26] on the properties of the resulting films and devices. In addition to the chemical composition of the sol, another strategy to achieve improved PSC device performance is represented by the use of ZnO nanocomposite films as ETLs. In particular, ZnO–polymer,[27] ZnO–reduced graphene oxide–polymer,[28] ZnO–fullerene derivative,[29,30] and ZnO–CdS[31] hybrid ETLs have been successfully demonstrated for both ZnO growth control and enhanced electron collection ability. Finally, another deeply investigated critical parameter in the formation of ZnO films as ETLs for PSC applications is the annealing temperature (T_A) of the as-deposited gel.[22,32–35] In particular, several works reported the effect of different T_A on the photovoltaic response of PSCs, showing that relatively high T_A (usually above 200 °C) are necessary to promote crystallization, maximize removal of organic residues and yield high device efficiency.[21,25,36,37] On the other hand, recent reports have also demonstrated the formation of amorphous ZnO films upon lower-temperature annealing treatments ($T_A \leq 150$ °C) and their incorporation in highly efficient PSCs,[7,8,14,23,38,39] thus paving the way for the application of this technology also to flexible devices fabricated onto heat-sensitive plastic substrates (*e.g.*, polyethylene terephthalate – PET).

From a chemical standpoint, the formation of the ZnO film is the result of a complex sequence of interconnected reactions that are at the basis of the two fundamental steps regulating the entire sol–gel process, namely hydrolysis of the metal precursor and subsequent condensation to form the ZnO network.[32] Despite the key role played by these two interplaying processes in the production of the final ZnO thin solid film, their influence on the functional properties of the resulting PSCs has been surprisingly overlooked.[33] In particular, no examples of systematic approaches to control and ultimately promote the hydrolysis and condensation steps during the formation of ZnO ETLs *via* sol–gel process have been presented in the literature to date, notwithstanding their potential to further improve PSC device efficiency.

Accordingly, a new approach is proposed in this work to favor the hydrolysis and condensation reactions in sol–gel derived ZnO ETL films, based on the systematic investigation of the effect of water concentration in the formulation of the sol–gel precursor on the performance of inverted PSCs. Such ZnO films were obtained upon low-temperature (140 °C) thermal treatments and were incorporated in rigid PSC devices. A thorough characterization of the obtained ZnO ETLs highlighted the key role played by water molecules in the starting sol formulation in favoring the formation of a ZnO network that is beneficial for improved device performance. In addition, the effect of such water content in the sol–gel precursor on the long-term stability of flexible PSC devices was also investigated. To the best of our knowledge, this study represents the first demonstration of effective control of ZnO sol–gel chemistry to achieve improved PSC performance at processing temperatures compatible with flexible plastic substrates.

Experimental

Synthesis of ZnO precursor solution and film preparation

All reagents were purchased from Sigma Aldrich unless otherwise stated. Different ZnO sol–gel precursor formulations were prepared by dissolving zinc acetate dihydrate $Zn(CH_3COO)_2 \cdot 2H_2O$ (ZAD, 0.5 M) and monoethanolamine $NH_2CH_2CH_2OH$ (MEA, 0.5 M) in 2-methoxyethanol $CH_3OCH_2CH_2OH$ (2-ME), with increasing amounts of additional water moles. In particular, three different water-to-zinc molar ratios ($r = [H_2O]/[Zn^{2+}]$) were considered, namely 2, 4 and 6 (with $r = 2$ indicating the reference formulation in which no additional water moles were present). The solutions were vigorously stirred at room temperature for 16 h in a closed vial. Then, the ZnO precursor solutions were spin coated onto the target substrates (glass, glass–ITO, and polyethylene terephthalate (PET)–ITO) at 1200 rpm for 40 s. Immediately after deposition, the films were placed onto a hot plate for the annealing step (140 °C, 1 h). The whole experimental procedure, from sol synthesis to film and device fabrication and characterization was conducted at a controlled relative humidity (RH) of 45–50% (except for the steps carried out in glove-box).

Fabrication of inverted PSCs

Inverted PSCs were fabricated on ITO-coated glass (surface resistivity 8–2 Ω sq^{-1}) and ITO-coated PET (surface resistivity 60 Ω sq^{-1}) substrates, both patterned in a nitro-hydrochloric acid solution. Prior to use, the substrates were ultrasonically cleaned in successive baths with de-ionized water, acetone, and isopropyl alcohol (IPA) and subsequently treated by oxygen plasma for 5 min at 150 W. The ZnO precursor solutions were deposited and thermally treated as previously reported. Subsequently, the ZnO-coated substrates were transferred into a nitrogen filled glovebox

for the deposition of the active layer, prepared with a 40 mg mL^{-1} solution of regioregular poly-3-hexylthiophene (P3HT, Rieke Metals):[6.6]-phenyl-C_{61}-butyric acid methyl ester (PCBM, Solenne BV) in 1,2-dichlorobenzene (DCB) and stirred for about 20 h at 50 °C. The P3HT : PCBM ratio was 1 : 1 by weight. The blend solution was spin coated at 700 rpm for 60 s and the wet films were covered with a Petri dish for solvent annealing (approximately 30 min).[34] The film thickness of the active layer was approximately 230 nm. PEDOT:PSS (Orgacon EL-P 5015, Agfa) was screen printed as HTL on top of the IPA-pre-wetted photoactive layer with a custom-built screen printing unit. The printing procedure was carried out in air with a 325 mesh screen, producing a 1 μm-thick HTL. After printing, the samples were thermally treated on a hotplate at 110 °C for 10 min in glovebox. Finally a silver grid as back-electrode was screen printed in air through a 325 mesh screen to complete the devices, using a commercially available silver paste (DuPont PV410) followed by thermal annealing in glove-box at 140 °C for 10 min. The active area of all fabricated devices was 0.40 cm^2. At least six devices were fabricated and tested for each examined condition.

Characterization

The current density–voltage (*J–V*) characteristics were recorded using a Keithley 2612B source-measure unit by illuminating the PSC devices with a 100 mW cm^{-2} AM 1.5G solar simulator (Sun 2000 Class A, Abet Technologies) calibrated by means of a NREL certified reference cell (PVMeasurements).

Fourier-transform infrared spectroscopy (FTIR) measurements were carried-out in transmission mode at room temperature using a Nicolet 760-FTIR (64 accumulated scans at a resolution of 4 cm^{-1} in the 4000–800 cm^{-1} wavenumber range). The ZnO thin films used for FTIR characterization were spin cast onto KBr disks using the deposition conditions previously described.

X-ray photoelectron spectroscopy (XPS) measurements were performed on ZnO films deposited on glass slides using an M-probe apparatus (Surface Science Instruments). Monochromatic Al Kα radiation (1486.6 eV) was used as source. Survey analysis in the whole range of X-ray spectra and high-resolution analysis in the typical regions of C-bonds, O-bonds, and Zn-bonds were registered. The 1s energy level of carbon (284.6 eV) was taken as the internal reference for peak shift corrections.

The transmittance spectra of ZnO thin films were recorded using an Evolution 600 (Thermo Scientific) ultraviolet-visible (UV-Vis) spectrophotometer in the 250–700 nm wavelength range. The photoluminescence spectra were obtained on solid ZnO films using a Jasco FP-6600 Spectrofluorometer. The excitation wavelength was 325 nm. The surface morphology and roughness of the ZnO thin films deposited on ITO-coated glass substrates were obtained by means of a NSCRIPTOR™ (Nanoink) atomic force microscope (AFM) in tapping mode.

Results and discussion

To evaluate the effect of chemical composition of the sol–gel precursor on the hydrolysis and condensation reactions occurring during film formation and on the final properties of ZnO ETL in PSC systems, different ZnO sol–gel precursor formulations were prepared and characterized. The commonly used sol precursor based on ZAD and MEA dissolved in 2-ME was modified by addition of increasing amounts of water in the starting formulation, to yield three different water-to-Zn molar ratios ($r = [H_2O]/[Zn^{2+}]$). For convenience, throughout the text ZnO thin films produced using *r* values of 2, 4, and 6 will be referred to as ZnO-*r*2, ZnO-*r*4, and ZnO-*r*6, respectively. Deposition of the solutions was followed by heat treatment at 140 °C for 1 h, resulting in the formation of amorphous films (see Fig. S1 in ESI† for XRD analysis). Such low-temperature annealing conditions for the ZnO layer were chosen to make this process compatible with the use of flexible plastic substrates (PET) for PSC fabrication without negatively affecting the mechanical, optical or functional properties of PET.[35]

A preliminary FTIR analysis was conducted on ZnO thin films processed from precursors at different *r* values to evaluate the effect of water content in the sol on the chemical structure of the resulting solid film (see Fig. 1).[18,23,36–39] In addition to the characteristic bands associated with the presence of water and hydroxyl groups, all spectra present several signals that can be ascribed to the presence of organic residues and byproducts in the formed ZnO films, although with different absorption intensities, as will be discussed hereafter. More specifically, a broad peak in the 3600–3000 cm^{-1} region is observed irrespective of the *r* value considered which is typically associated with the stretching vibrations of O–H bonds and that indicates the presence of hydroxyl groups (from MEA, 2-ME and zinc hydroxide) and water molecules in the ETL film. A first clear evidence of the presence of organic byproducts in the films is given by the weak signals found in the 3000–2800 cm^{-1} range that may be attributed to symmetric/asymmetric stretching vibrations of CH bonds in methyl and methylene groups, respectively.[37] The region in the 1600–1300 cm^{-1} range is often considered as the fingerprint of the organic byproducts originating from uncomplete elimination of acetate groups in ZAD upon hydrolysis and condensation. In particular, the peaks centred at 1575 cm^{-1} and 1403 cm^{-1} may be associated with

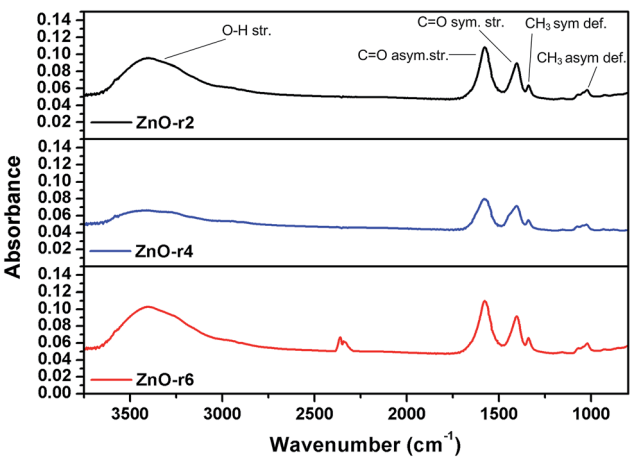

Fig. 1 FTIR spectra of ZnO-*r*2, ZnO-*r*4, and ZnO-*r*6 thin films.

carboxylate asymmetric and symmetric C=O stretching modes, respectively.[18] In addition to such species, other prominent features can be observed in the FTIR spectra that can be related to organic residues originating from 2-ME and MEA. In particular the bands centred at 1341 cm^{-1} and 1022 cm^{-1} may be assigned to symmetric and asymmetric deformations of methylene groups in 2-ME and ZAD.[36] The stretching mode of the N–H bond at 1420 cm^{-1}, associated to residual MEA, is mainly superimposed with the signal attributed to stretching vibrations of the C=O bond in the acetate group of ZAD. The presence of residues originating from MEA may also be responsible for the weak shoulder at 3250 cm^{-1}.[40] Additionally, residual traces of MEA may be also correlated to the weak signal found at 1156 cm^{-1} that can be associated with the stretching mode of C–N bonds.[18]

Based on these considerations, a semi-quantitative analysis of the abundance of the chemical groups in the films (60 nm thick, as measured by means of surface profilometry) was carried out by evaluating the relative absorption intensities of the signals present in the FTIR spectra at varying *r* values. Because the $[H_2O]/[Zn^{2+}]$ ratio in the starting formulation was not shown to affect the thickness of the deposited ZnO layer (see Fig. S2 in ESI†), a comparative analysis may be performed. Results revealed a marked decrease in the intensity of the peaks associated to the organic moieties related to the acetate groups (carboxylate $C{=}O_{asym\ str}$ and $C{=}O_{sym\ str}$ at 1575 cm^{-1} and 1403 cm^{-1}, respectively) in ZnO-*r*4, compared to ZnO-*r*2 and ZnO-*r*6 (see Table S1 in ESI† for calculations). These trends suggest a decreased amount of residual acetate groups in ZnO-*r*4, likely indicating improved elimination of these moieties during the hydrolysis and condensation reactions upon addition of supplementary H_2O moles to the starting formulation. A further increase in the $[H_2O]/[Zn^{2+}]$ ratio to 6 leads to a slight increase in the signal relative intensities in the 1600–1400 cm^{-1} region, although to a lower extent than what found in ZnO-*r*2. This behavior may be correlated to the chemistry of the hydrolysis process, as will be discussed in detail in the next paragraphs.

In order to better clarify the trends observed with FTIR analysis, X-ray photoelectron spectroscopy (XPS) was performed on all ZnO films obtained from formulations with increasing water-to-zinc molar ratios and the results are presented in Fig. 2. The atomic concentration of the surface chemical species extrapolated from the XPS survey spectra (Fig. 2a) showed a reduction of carbon concentration in the ZnO films for increasing *r* values.

In particular, the carbon concentration was found to decrease from 42.7% to 32.8% ($\%_{at}$) with increasing $[H_2O]/[Zn^{2+}]$ molar ratio from $r = 2$ to $r = 4$. In addition a further increase in the *r* value from 4 to 6 led to a slight increase in atomic carbon concentration up to 35.1%. To gain additional insights into the presence of organic byproducts and unreacted moieties on the ZnO films, high-resolution XPS spectra of C 1s core levels were investigated (Fig. 2b). The C 1s spectra are characterized by the presence of two peaks centred at 284.6 eV and 288.5 eV, respectively. The peak at lower binding energy located at 284.6 eV can be associated to C–C or C–H bonds,[41] whereas the peak at higher binding energy located at 288.5 eV can be associated to C=O bonds.[23,42] As shown in Fig. 2b, a clear decrease in the intensity of the peak at higher binding energy is observed for ZnO films obtained from formulation with higher $[H_2O]/[Zn^{2+}]$ molar ratios (ZnO-*r*4 and ZnO-*r*6). Such trend in the high-resolution spectra of C 1s core levels may be correlated to a reduction of the concentration of acetate groups in the ZnO films for increasing H_2O concentration in the starting formulation, as also observed from FTIR analysis. Fig. 2c shows the high-resolution XPS spectra of O 1s core levels for the ZnO films obtained at increasing $[H_2O]/[Zn^{2+}]$ molar ratio. The experimental data were fitted with a Gaussian function (solid lines in Fig. 2c) whose deconvolution highlighted the presence of two distinct peaks (dashed lines in Fig. 2c). The peak at lower binding energy centred at 529.8 eV can be attributed to the O^{2-} ions in the ZnO structure,[43,44] whereas the peak at higher binding energy centred at 531.5 eV can be associated with the O^{2-} ions in oxygen deficient states such as in $Zn(OH)_2$ (ref. 45) and with oxygen bound to carbon atoms originated from organic byproducts.[24] The spectra clearly show an increase in the relative magnitude of the lower binding energy peak for ZnO-*r*4 and ZnO-*r*6 compared with ZnO-*r*2, accompanied by a decrease of the higher binding energy signal. In particular, the atomic ratios of the 529.8 eV signal to the 531.5 eV signal were calculated to be 0.81, 1.23, and 1.12 for ZnO-*r*2, ZnO-*r*4, and ZnO-*r*6, respectively. These trends suggest that the presence of additional H_2O moles in the sol–gel precursor formulation may promote a more efficient formation of Zn–O bonds in the ZnO film, thus leading to a reduction of the concentration of oxygen deficient species and of oxygen associated with organic residues and non-eliminated byproducts. This behavior may beneficially affect the functional properties of such ZnO films when incorporated as ETL in working photovoltaic devices, as will be discussed in detail in the following. Finally, the high-resolution XPS spectra of Zn $2p_{3/2}$ core levels are also reported in Fig. 2d. One single symmetric peak located at binding energy of 1021.1 eV is found in all samples, irrespective of the composition of the sol–gel formulation.

Based on the results obtained from FTIR and XPS analyses, it clearly appears that the composition of the starting sol precursor formulation in terms of varying $[H_2O]/[Zn^{2+}]$ concentration ratio can significantly influence the chemical structure of the resulting sol–gel based ZnO thin films. More specifically, such an increase in H_2O content may lead to improved dissolution of Zn^{2+} ions in the sol due to the higher dielectric constant of water if compared to that of 2-ME,[46] thus resulting in more Zn^{2+} ions available for reaction to form the $(Zn–O–Zn)_n$ 3D network in the solid film. Furthermore, such water addition may promote the hydrolysis step of zinc acetate to form $Zn(OH)_2$ intermediates that yield the final ZnO solid film upon successive condensation (Scheme 1).

The elimination of water and acetic acid ($T_b = 118$ °C) is allowed by the mild thermal annealing treatment, conducted after sol deposition at 140 °C. As shown in Scheme 2, upon addition of supplementary moles of water in the formulation of the starting sol, the chemical equilibrium of the hydrolysis reaction may be shifted in the direction of the hydrolysis step (green arrow). This pathway may be correlated with the decrease

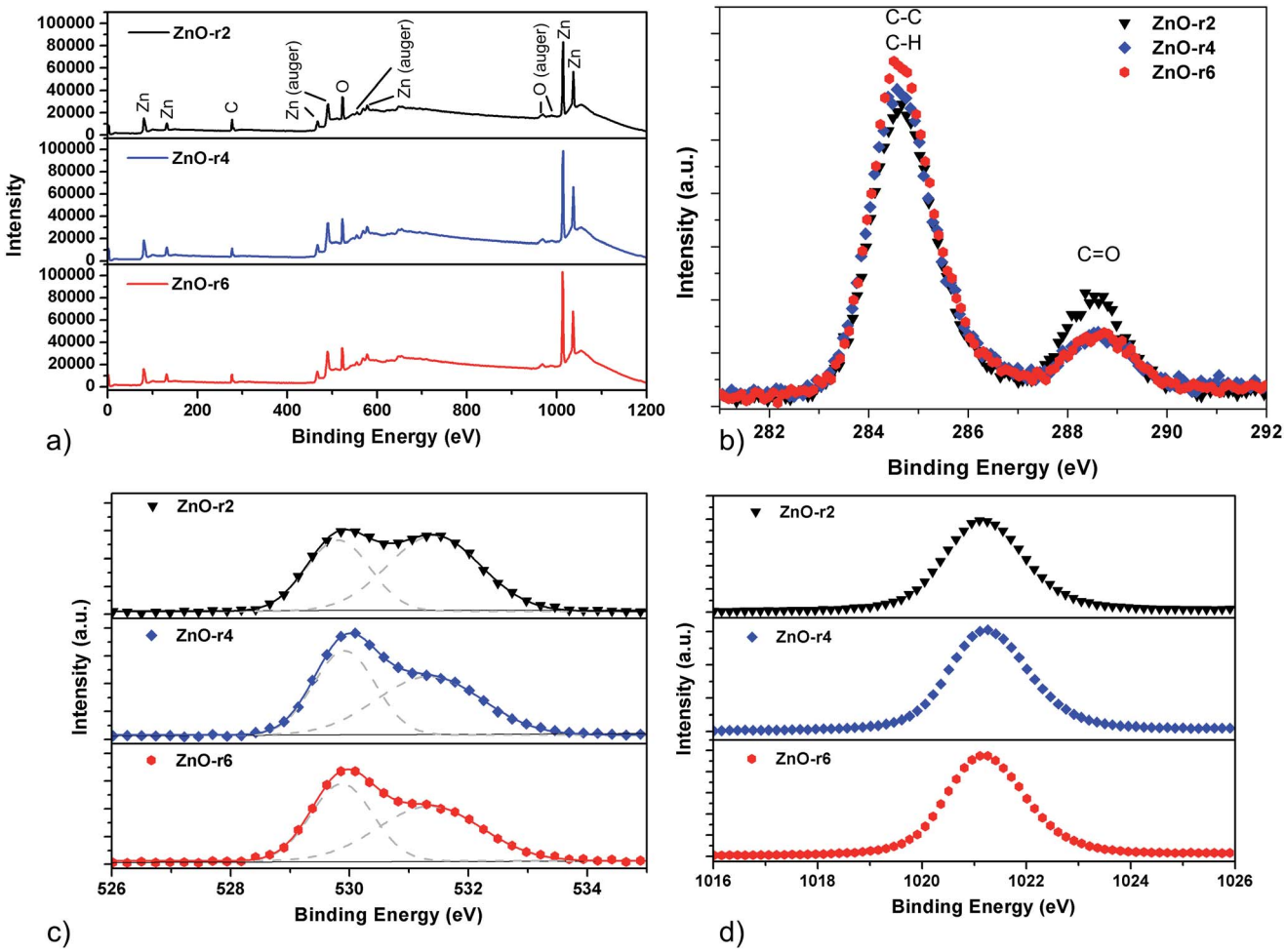

Fig. 2 (a) XPS survey spectra and high-resolution XPS spectra of (b) C 1s, (c) O 1s, and (d) Zn $2p_{3/2}$ core levels of ZnO-*r*2, ZnO-*r*4, and ZnO-*r*6 thin films.

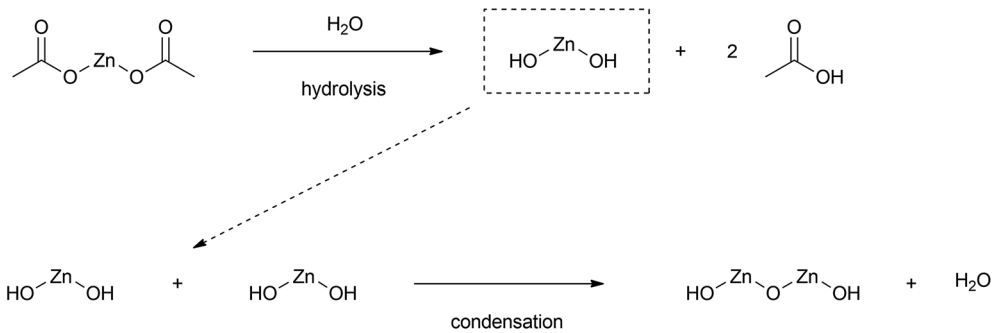

Scheme 1 Schematic representation of hydrolysis and condensation reactions involved in the sol–gel process to form a solid ZnO film starting from zinc acetate as the metal precursor.

of FTIR absorption intensity of the peaks associated to carboxylate C=O (symmetric and asymmetric) stretching vibrations in acetate groups. In addition, it can also explain the intensity decrease of the O–H stretching signals in the FTIR spectrum (Fig. 1) that results from further release of OH groups as a consequence of the hydrolysis step. These results are corroborated by the XPS analysis (Fig. 2) that evidenced both a decrease in the atomic concentration of carbon related to acetate residues in the ZnO films as well as a more efficient formation of the $(Zn–O–Zn)_n$ solid network. As opposed to this, a lower $[H_2O]/[Zn^{2+}]$ ratio in the sol formulation may yield the formation of relatively complicated reaction precursors,[47] such as Zn-oxo-acetate or Zn-hydroxo-acetate species, characterized by the presence of intercalated acetate and hydroxyl groups

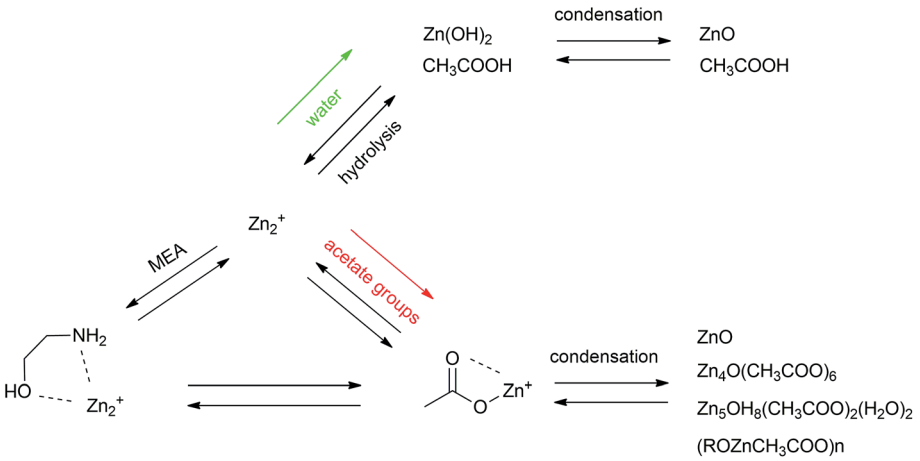

Scheme 2 Schematic representation of the chemical equilibria involved in the ZnO sol–gel process.

strongly bound to Zn^{2+} and thus more difficult to be removed at low temperatures (140 °C), as shown by the reaction pathway in Scheme 2 (red arrow). These considerations are supported by the evidence of a higher concentration of acetate groups in ZnO films produced starting from a precursor formulation with lower water concentration (ZnO-*r*2), as inferred from both FTIR and XPS analyses.

By further increasing the $[H_2O]/[Zn^{2+}]$ molar ratio in the precursor solution from 4 to 6, an increase in concentration of organic residues and byproducts in the ZnO film was observed as suggested by XPS and FTIR analyses (Fig. 1 and 2). These results may imply that the addition of an excessive amount of water ($r > 4$) in the sol–gel precursor formulation leads to an excessive formation of acetic acid during the hydrolysis step that destabilizes the sol and shifts the reaction equilibrium back to the formation of Zn-oxo-acetate or Zn-hydroxo-acetate species that are found to persist within the solid film even after thermal treatment. In particular, higher water concentrations ($r > 6$) were found to determine significant sol instabilities and immediate precipitation after preparation (see Fig. S3 in ESI†).

The optical properties of the sol–gel based ZnO thin films produced from precursors at different *r* values were investigated by collecting their transmittance spectra, as reported in Fig. 3a.

All ZnO thin films showed comparable optical properties over the entire visible wavelength range with an average optical transmittance of about 89%, thus indicating limited parasitic absorption that could negatively affect charge generation in the photoactive layer. As a result, the $[H_2O]/[Zn^{2+}]$ molar ratio in the sol–gel precursor was not found to significantly affect the optical properties of the sol–gel based ZnO thin films.

In order to gain further insights into the surface properties of the as-prepared ZnO thin films, fluorescence emission spectroscopy was carried out on films obtained from precursor formulations with increasing $[H_2O]/[Zn^{2+}]$ molar ratio (see Fig. 3b). A characteristic emission band in the 350–400 nm region was observed in all fluorescence spectra, typical of the band-edge emission of ZnO in the UV-region. In addition, another broad absorption feature was found in the 400–500 nm spectral range, which was reported to be correlated with the electronic transitions associated with the presence of Zn surface defects and surface states in the ZnO film.[30,31] As shown in

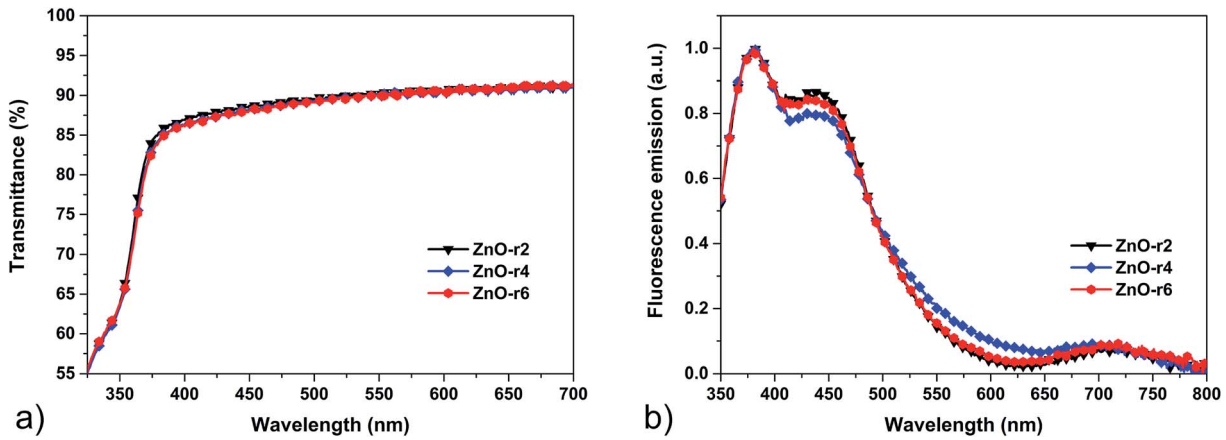

Fig. 3 (a) Optical transmittance spectra and (b) fluorescence emission spectra of ZnO-*r*2, ZnO-*r*4, and ZnO-*r*6 thin films.

Fig. 3b, the emission intensity of such peak was found to be slightly lower for ZnO-*r*4 thin films compared to ZnO-*r*2 and ZnO-*r*6, likely indicating that for this formulation the charge carrier recombination processes due to the presence of such surface defects and states can be minimized. These trends well agree with the results obtained from the FTIR and XPS analyses discussed above.

In order to investigate the possible effect of water content in the sol precursor formulation on the surface morphology of sol–gel based ZnO thin films, topographic AFM images were recorded, as shown in Fig. 4.

All the ZnO thin films presented similar surface morphology characterized by a wrinkled texture, formed by fiber-like domains likely originating from the interactions between the intermediate species during the gelation process occurring immediately after the spin coating deposition.[9,48] Moreover, the surface root mean square roughness of the films obtained at varying $[H_2O]/[Zn^{2+}]$ ratios showed comparable values (see Table S2 in ESI†), suggesting that the presence of additional water molecules in the precursor solution does not appear to significantly affect the fiber-like texture of the resulting ZnO thin films.

In order to investigate the effect of water concentration in the starting ZnO sol formulation on the functional response of operating devices, inverted PSCs incorporating sol–gel derived ETLs obtained from ZnO-*r*2, ZnO-*r*4, and ZnO-*r*6 were fabricated and tested. The corresponding *J*–*V* characteristics are reported in Fig. 5 and the associated average photovoltaic parameters are shown in Table 1.

PSC devices incorporating a ZnO-*r*2 ETL showed a V_{oc} of 563 mV, a J_{sc} of 5.01 mA cm^{-2}, a FF of 45.9%, and a PCE of 1.29%. When the $[H_2O]/[Zn^{2+}]$ molar ratio was doubled in the starting ZnO formulation (from 2 to 4), a clear increase in photovoltaic performance was observed. In particular J_{sc} was found to increase of about 16% (from 5.01 mA cm^{-2} to 5.82 mA cm^{-2}), accompanied by a simultaneous increase in FF (from 45.9% to 49.8%), resulting in an overall 25% increase in PCE (from 1.29% to 1.62%). Such improved efficiencies are comparable to those observed in the scientific literature for similar systems in spite of the different processing techniques adopted in this work for the printing of both HTL and silver back electrode.[49–51] A further increase in water concentration in the starting ZnO sol formulation (ZnO-*r*6) was shown to cause a decrease in the photovoltaic performance of devices, leading to V_{oc}, J_{sc}, FF and PCE values of 567 mV, 5.19 mA cm^{-2}, 44.3% and 1.31%, respectively. These trends characterized by the presence of a maximum device efficiency for devices incorporating a ZnO-*r*4 ETL are largely associated with the changes in current density of PSC devices for increasing *r* values. These modification in J_{sc} may in turn be related to the amount of residual acetate groups leaving the ZnO film during the hydrolysis and condensation steps, as previously discussed based on the presented FTIR and XPS analyses. Indeed, promoting the release of insulating acetate groups from the forming ZnO film is expected to enhance the electron extraction ability of the ETL by limiting detrimental phenomena such as recombination or trapping of charge carriers.[23,33] Furthermore, the lower leakage current extrapolated from the *J*–*V* characteristics in the dark (see Fig. S4 in ESI†) corroborated these considerations, thus confirming the better charge selectivity of PSCs incorporating ZnO-*r*4 compared to ZnO-*r*2 and ZnO-*r*6. Moreover, such improved device performance for ZnO-*r*4 may also be related to the promoted conversion of zinc acetate to zinc oxide as confirmed by the increased concentration of Zn–O bonds in the sol–gel based ETL

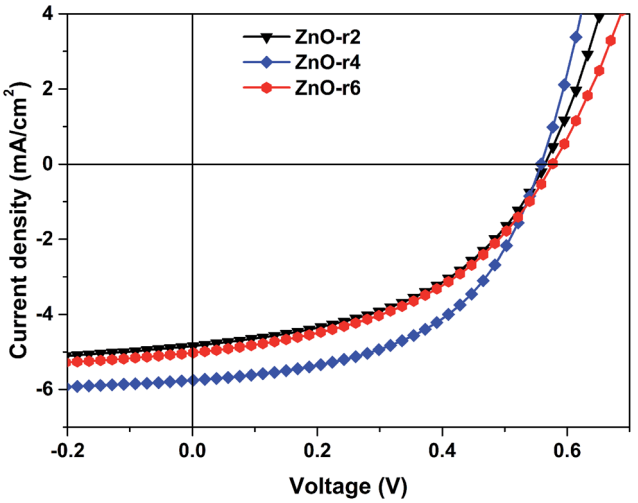

Fig. 5 *J*–*V* characteristics of inverted PSCs incorporating sol–gel based ZnO-*r*2, ZnO-*r*4, and ZnO-*r*6 ETLs.

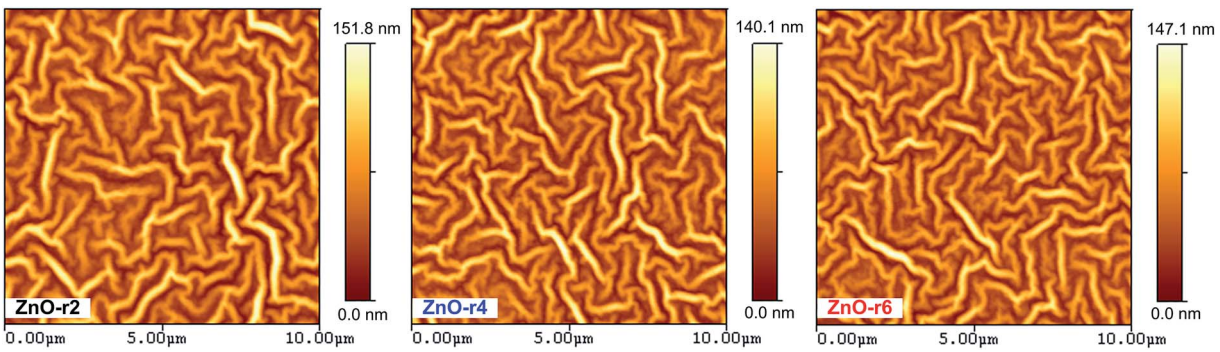

Fig. 4 Topographic AFM images of ZnO-*r*2, ZnO-*r*4, and ZnO-*r*6 thin films.

Table 1 Average photovoltaic parameters of rigid inverted PSCs incorporating sol–gel based ZnO-*r*2, ZnO-*r*4, and ZnO-*r*6 ETLs

Sample	V_{oc} [mV]	J_{sc} [mA cm^{-2}]	FF [%]	PCE [%]	R_s [Ω cm^2]	R_{sh} [Ω cm^2]
ZnO $r = 2$	563 ± 5	5.01 ± 0.29	45.9 ± 1.3	1.29 ± 0.11	29 ± 3	543 ± 26
ZnO $r = 4$	558 ± 8	5.82 ± 0.34	49.8 ± 2.1	1.62 ± 0.11	21 ± 5	774 ± 68
ZnO $r = 6$	567 ± 7	5.19 ± 0.23	44.3 ± 1.8	1.31 ± 0.06	32 ± 9	586 ± 78

evidenced by the high-resolution XPS spectra of O 1s core levels (Fig. 2c).

It is worth pointing out that the release of acetate groups from the forming sol–gel based ZnO thin film promoted by the presence of additional water molecules in the starting formulation could lead to appropriate modifications of the electronic properties of the ETL. In fact, it is known from the literature that the presence of organic unreacted residues on the ZnO thin film surface may yield an increase in the work-function of the ZnO layer due to surface dipole effects.[52] Therefore, lowering the concentration of such organic residues on the ZnO surface by chemically controlling the sol–gel process is expected to lead to a corresponding work-function decrease of the ZnO ETL. In turn, this is likely to promote a better energy level alignment within the device stack that leads to improved extraction and injection of the charge carriers and to enhanced device performance.[30] Moreover, electrical measurements were also attempted on ZnO films, but unfortunately they did not prove useful to gain further insights into these aspects (see ESI† for details).

The PCE decrease observed by further increasing the $[H_2O]/[Zn^{2+}]$ molar ratio in the ZnO precursor solution (from 4 to 6) may be correlated with the corresponding decreased concentration of Zn–O bonds in the formed film as observed from XPS analysis, in addition to a higher concentration of organic byproducts and residues (Zn-oxo-acetate and Zn-hydroxo-acetate species, see Scheme 2) still present in the ZnO films even after thermal treatment. The presence of relatively fewer Zn–O–Zn bonds together with an increased amount of such organic species increases the probability of charge trapping and recombination, thus resulting in lower photovoltaic performance.

Ascertained the importance of controlling the chemistry of the sol–gel process in order to optimize the functional performance of the ZnO ETL in PSC devices, the effect of $[H_2O]/[Zn^{2+}]$ ratio on the stability of devices was evaluated. To this end, flexible PSCs incorporating ZnO-*r*2, ZnO-*r*4, and ZnO-*r*6 were fabricated onto PET substrates (Fig. 6, inset), the latter being compatible with the low-temperature annealing process (140 °C) specifically chosen in this work for the heat treatment of the ZnO ETL. Such flexible devices were then aged for over 1000 h in a nitrogen environment without encapsulation. In this way, the potential interplay of water in the starting ZnO sol formulation and atmospheric water onto device stability could be confined during the aging test and the sole effect on performance stability of the presence of water in the ZnO sol–gel formulation could be investigated. As shown in Fig. 6, after more than 1000 h of shelf-life tests, all flexible PSCs retained more than 80% of their initial efficiency, thus revealing relatively good stability. It

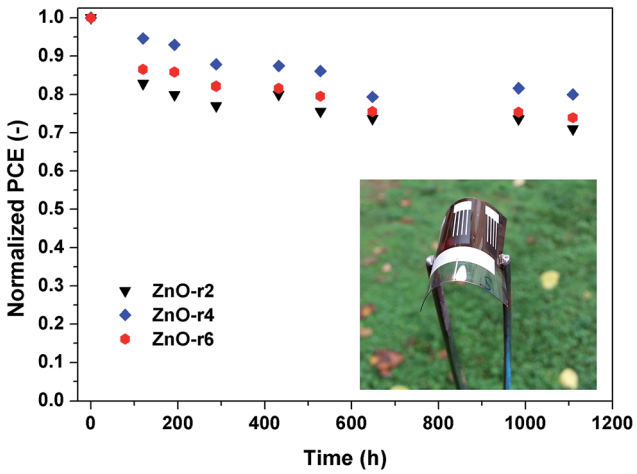

Fig. 6 Normalized PCEs of flexible devices as a function of the aging time in nitrogen atmosphere without encapsulation.

is worth mentioning that for the evaluation of device performance upon aging time, all devices were briefly exposed to atmospheric conditions during the *J*–*V* tests. In addition, fabrication of the devices was mostly carried out in air. Both these experimental conditions may have impacted on the overall long term stability of all PSCs, irrespective of the composition of the starting ZnO sol formulation.

Interestingly, devices incorporating the ZnO-*r*4 ETL exhibited relatively higher stability compared to ZnO-*r*2 and ZnO-*r*6. This behavior may be correlated with the improved chemical conversion of the ZnO precursor and with the promoted release of acetate groups and water during the annealing step as observed from FTIR and XPS in ZnO-*r*4 (Fig. 1 and 2). In particular, the lower concentration of organic residues and byproducts in the ZnO ETL may induce the formation of a more favorable ETL/BHJ interface that may help limit the potentially detrimental interactions of such organic residues with the photoactive material upon aging (morphological rearrangements, photochemical degradation), thus resulting in improved device stability.

Conclusion

A systematic investigation was presented in this work on the effect of the chemical composition of the ZnO sol–gel precursor on the formation of ZnO-based thin films used as ETL in inverted PSC devices. Different $[H_2O]/[Zn^{2+}]$ molar ratios were investigated in the starting sol formulation ($r = 2, 4, 6$) and their influence on film properties and device performance was

elucidated. FTIR and XPS analyses highlighted the key importance of the judicious control over the $[H_2O]/[Zn^{2+}]$ molar ratio in the starting sol formulation to promote the sol–gel hydrolysis and condensation steps, suggesting that excessive water concentration may lead to instabilities in the precursor solution with subsequent precipitation upon sol preparation. Based on FTIR and XPS results, a mechanism for the formation of the ZnO film at the low processing temperatures used in this work was proposed. PSC devices were fabricated incorporating ZnO ETLs obtained from sol precursor formulations with increasing $[H_2O]/[Zn^{2+}]$ ratios and the corresponding *J–V* tests revealed the presence of a maximum device efficiency for intermediate $[H_2O]/[Zn^{2+}]$ molar ratios (ZnO-*r*4) in the starting ZnO formulation. This behavior was found to well correlate with XPS and FTIR results, in which a clear decrease of concentration of organic byproducts and residues (mainly acetate and oxo-acetate groups) was observed for ZnO-*r*4. By promoting the release of electrically insulating acetate groups from the forming ZnO film, the electron extraction ability of the ETL is enhanced by limiting detrimental phenomena such as recombination or trapping of charge carriers. As a result, improved device performance was observed. Finally, the effect of $[H_2O]/[Zn^{2+}]$ molar ratio on the shelf-life of PSCs fabricated onto flexible PET substrates was investigated. All flexible devices were shown to retain more than 80% of their initial efficiency upon aging in a nitrogen environment for more than 1000 h, thus revealing relatively good stability. In addition, PSCs incorporating the ZnO-*r*4 ETL exhibited relatively higher stability compared to ZnO-*r*2 and ZnO-*r*6. This behavior was correlated with the improved chemical conversion of the ZnO precursor and with the promoted release of acetate groups and water during the annealing step as observed from FTIR and XPS that may limit the detrimental interactions between unreacted ZnO precursor residues and the photoactive material upon aging, thus resulting in improved device stability.

In conclusion, the results of this study give the first clear demonstration of a viable and straightforward way to achieve improved PSC performance at processing temperatures compatible with flexible plastic substrates *via* the effective control of the ZnO sol–gel chemistry.

References

1 F. C. Krebs, *Org. Electron.*, 2009, **10**, 761–768.
2 D. Angmo, S. A. Gevorgyan, T. T. Larsen-Olsen, R. R. Søndergaard, M. Hösel, M. Jørgensen, R. Gupta, G. U. Kulkarni and F. C. Krebs, *Org. Electron.*, 2013, **14**, 984–994.
3 R. R. Søndergaard, M. Hösel and F. C. Krebs, *J. Polym. Sci., Part B: Polym. Phys.*, 2013, **51**, 16–34.
4 Y. Liu, T. T. Larsen-Olsen, X. Zhao, B. Andreasen, R. R. Søndergaard, M. Helgesen, K. Norrman, M. Jørgensen, F. C. Krebs and X. Zhan, *Sol. Energy Mater. Sol. Cells*, 2013, **112**, 157–162.
5 G. Iannaccone, M. Välimäki, E. Jansson, A. Sunnari, G. Corso, A. Bernardi, M. Levi, S. Turri, J. Hast and G. Griffini, *Sol. Energy Mater. Sol. Cells*, 2015, **143**, 227–235.
6 S. Lattante, *Electronics*, 2014, **3**, 132.
7 R. Po, C. Carbonera, A. Bernardi and N. Camaioni, *Energy Environ. Sci.*, 2011, **4**, 285–310.
8 Y. Sun, J. H. Seo, C. J. Takacs, J. Seifter and A. J. Heeger, *Adv. Mater.*, 2011, **23**, 1679–1683.
9 H.-Y. Park, D. Lim, K.-D. Kim and S.-Y. Jang, *J. Mater. Chem. A*, 2013, **1**, 6327–6334.
10 L. V. Podrezova, S. Porro, V. Cauda, M. Fontana and G. Cicero, *Appl. Phys. A*, 2013, **113**, 623–632.
11 R. Hong, H. Qi, J. Huang, H. He, Z. Fan and J. Shao, *Thin Solid Films*, 2005, **473**, 58–62.
12 F. D. Paraguay, W. L. Estrada, D. R. N. Acosta, E. Andrade and M. Miki-Yoshida, *Thin Solid Films*, 1999, **350**, 192–202.
13 J. S. Wellings, N. B. Chaure, S. N. Heavens and I. M. Dharmadasa, *Thin Solid Films*, 2008, **516**, 3893–3898.
14 S. J. Lim, S. Kwon and H. Kim, *Thin Solid Films*, 2008, **516**, 1523–1528.
15 H.-C. Cha, Y.-C. Huang, F.-H. Hsu, C.-M. Chuang, D.-H. Lu, C.-W. Chou, C.-Y. Chen and C.-S. Tsao, *Sol. Energy Mater. Sol. Cells*, 2014, **130**, 191–198.
16 F. C. Krebs, S. A. Gevorgyan and J. Alstrup, *J. Mater. Chem.*, 2009, **19**, 5442–5451.
17 Y.-J. Kang, K. Lim, S. Jung, D.-G. Kim, J.-K. Kim, C.-S. Kim, S. H. Kim and J.-W. Kang, *Sol. Energy Mater. Sol. Cells*, 2012, **96**, 137–140.
18 L. Znaidi, G. J. A. A. S. Illia, R. L. Guennic, C. Sanchez and A. Kanaev, *J. Sol-Gel Sci. Technol.*, 2003, **26**, 817–821.
19 L. Znaidi, *Mater. Sci. Eng., B*, 2010, **174**, 18–30.
20 J.-H. Lee, K.-H. Ko and B.-O. Park, *J. Cryst. Growth*, 2003, **247**, 119–125.
21 L. Armelao, M. Fabrizio, S. Gialanella and F. Zordan, *Thin Solid Films*, 2001, **394**, 89–95.
22 A. K. K. Kyaw, X. W. Sun, C. Y. Jiang, G. Q. Lo, D. W. Zhao and D. L. Kwong, *Appl. Phys. Lett.*, 2008, **93**, 221107.
23 R. Lin, M. Miwa, M. Wright and A. Uddin, *Thin Solid Films*, 2014, **566**, 99–107.
24 L. K. Jagadamma, M. Abdelsamie, A. El Labban, E. Aresu, G. O. Ngongang Ndjawa, D. H. Anjum, D. Cha, P. M. Beaujuge and A. Amassian, *J. Mater. Chem. A*, 2014, **2**, 13321–13331.
25 P. Morvillo, R. Diana, R. Ricciardi, E. Bobeico and C. Minarini, *J. Sol-Gel Sci. Technol.*, 2015, **73**, 550–556.
26 D. Barrera, Y.-J. Lee and J. W. P. Hsu, *Sol. Energy Mater. Sol. Cells*, 2014, **125**, 27–32.
27 C. E. Small, S. Chen, J. Subbiah, C. M. Amb, S.-W. Tsang, T.-H. Lai, J. R. Reynolds and F. So, *Nat. Photonics*, 2012, **6**, 115–120.
28 T. Hu, L. Chen, K. Yuan and Y. Chen, *Chem.–Eur. J.*, 2014, **20**, 17178–17184.
29 S.-H. Liao, H.-J. Jhuo, Y.-S. Cheng and S.-A. Chen, *Adv. Mater.*, 2013, **25**, 4766–4771.
30 T. Hu, L. Chen, K. Yuan and Y. Chen, *Nanoscale*, 2015, **7**, 9194–9203.
31 K. Yuan, L. Chen, F. Li and Y. Chen, *J. Mater. Chem. C*, 2014, **2**, 1018–1027.

32 C. J. Brinker and G. W. Scherer, *Sol-Gel Science: The Physics and Chemistry of Sol-Gel Processing*, Academic Press, Boston, 1st edn, 1990, .
33 P. Morvillo, R. Diana, A. Mucci, E. Bobeico, R. Ricciardi and C. Minarini, *Sol. Energy Mater. Sol. Cells*, 2015, **141**, 210–217.
34 G. Li, Y. Yao, H. Yang, V. Shrotriya, G. Yang and Y. Yang, *Adv. Funct. Mater.*, 2007, **17**, 1636–1644.
35 V. Zardetto, T. M. Brown, A. Reale and A. Di Carlo, *J. Polym. Sci., Part B: Polym. Phys.*, 2011, **49**, 638–648.
36 J. B. Miller, H.-J. Hsieh, B. H. Howard and E. Broitman, *Thin Solid Films*, 2010, **518**, 6792–6798.
37 T. Biswick, W. Jones, A. Pacuła, E. Serwicka and J. Podobinski, *Solid State Sci.*, 2009, **11**, 330–335.
38 E. Hosono, S. Fujihara, T. Kimura and H. Imai, *J. Sol-Gel Sci. Technol.*, 2004, **29**, 71–79.
39 J. S. Meena, M.-C. Chu, Y.-C. Chang, H.-C. You, R. Singh, P.-T. Liu, H.-P. D. Shieh, F.-C. Chang and F.-H. Ko, *J. Mater. Chem. C*, 2013, **1**, 6613–6622.
40 S. Bandyopadhyay, G. K. Paul, R. Roy, S. K. Sen and S. Sen, *Mater. Chem. Phys.*, 2002, **74**, 83–91.
41 W. Wang, Q. Feng, K. Jiang, J. Huang, X. Zhang, W. Song and R. Tan, *Appl. Surf. Sci.*, 2011, **257**, 3884–3887.
42 L. N. Bai, S. Wang, H. M. Sun, Q. Jiang and J. S. Lian, *Appl. Surf. Sci.*, 2014, **313**, 888–895.
43 M. Chen, X. Wang, Y. H. Yu, Z. L. Pei, X. D. Bai, C. Sun, R. F. Huang and L. S. Wen, *Appl. Surf. Sci.*, 2000, **158**, 134–140.
44 A. Sharma, J. B. Franklin, B. Singh, G. G. Andersson and D. A. Lewis, *Org. Electron.*, 2015, **24**, 131–136.
45 X. Q. Wei, B. Y. Man, M. Liu, C. S. Xue, H. Z. Zhuang and C. Yang, *Phys. Rev. B: Condens. Matter Mater. Phys.*, 2007, **388**, 145–152.
46 E. A. Meulenkamp, *J. Phys. Chem. B*, 1998, **102**, 5566–5572.
47 L. Znaidi, G. J. A. A. Soler Illia, S. Benyahia, C. Sanchez and A. V. Kanaev, *Thin Solid Films*, 2003, **428**, 257–262.
48 S. Seimei and M. Kimiaki, *Jpn. J. Appl. Phys.*, 2012, **51**, 095803.
49 T. Kuwabara, T. Nakashima, T. Yamaguchi and K. Takahashi, *Org. Electron.*, 2012, **13**, 1136–1140.
50 Y.-J. Kang, K. Lim, S. Jung, D.-G. Kim, J.-K. Kim, C.-S. Kim, S. H. Kim and J.-W. Kang, *Sol. Energy Mater. Sol. Cells*, 2012, **96**, 137–140.
51 D. Angmo, J. Sweelssen, R. Andriessen, Y. Galagan and F. C. Krebs, *Adv. Energy Mater.*, 2013, **3**, 1230–1237.
52 E. L. Ratcliff, A. K. Sigdel, M. R. Macech, K. Nebesny, P. A. Lee, D. S. Ginley, N. R. Armstrong and J. J. Berry, *Thin Solid Films*, 2012, **520**, 5652–5663.